Geometric Localization and the Quantum-Classical Transition

A Phenomenological Lindblad Model Constrained by Matter-Wave Interferometry and LISA Pathfinder

Anisse ZEROUTA

Abstract

We isolate and test a phenomenological quantum-localization sector motivated by a geometric-filtration hypothesis. The model assigns each maximal mechanically bound domain a local aperture scale r_d and a completely positive, translation-covariant localization generator. Its rate is $\Gamma_D = \gamma_0 (M/m_0)^\alpha \mathcal{F}_p(R/r_d)$, with $\mathcal{F}_p(z) = z^p/(1+z^p)$. The exponent p remains a model parameter; $p = 4$ is used only as the numerical benchmark. We derive the position-space coherence kernel, momentum diffusion, heating, composite-domain amplification, and interferometer transfer functions. The channel is then inserted into the deposited raw-count likelihood of the MUSCLE sodium-cluster Talbot-Lau experiment. A profile analysis of 95 scans and 3,895 points gives no statistically secure detection and yields the conditional conservative sensitivity value $\gamma_0 < 0.41\,\mathrm{s}^{-1}$ for $r_d = 25\,\mathrm{nm}$, $\alpha = 1$, and $p = 4$. Independently, the 2018 LISA Pathfinder differential-acceleration spectrum gives $\gamma_0 < 2.724 \times 10^{-4}\,\mathrm{s}^{-1}$ under the assumptions of a white Markovian channel, independent forces on the two test masses, and a single rigid localization domain per test mass. LISA Pathfinder is therefore stronger by a factor 1.486×10^3 at the benchmark, while the two constraints cross at $\alpha_* = 0.8546$. Experiment-specific checks for C60, a Rb-87 atom interferometer, and a Cs-133 fountain remain consistent with the stronger bound; the LUMI oligoporphyrin experiment is retained qualitatively because no unique primary structural radius is available. A first-order Talbot design reaches a geometric attenuation exponent of unity at a sodium-cluster diameter of 18.30 nm, corresponding to 1.88 MDa and $11.82\,\mathrm{m\,s}^{-1}$. All quoted upper values are conditional on the stated domain prescription and calibration model; the MUSCLE value uses an uncalibrated conventional profile criterion. They constrain this localization ansatz; they do not establish an underlying spacetime microstructure.

Affiliation: Precog Technologies - Theoretical Physics Division, Paris, France
Correspondence: a.zerouta@precogtec.com

1. Introduction

Quantum theory does not impose a fundamental size at which a material system must cease to display interference. In practice, increasingly massive and complex objects become difficult to isolate, and their observable coherence is reduced by collisions, thermal emission, electromagnetic coupling, vibrations, source dispersion, detector response, and other conventional mechanisms. Matter-wave experiments have nevertheless extended interference to large molecules, cold atomic ensembles, and, most recently, metal clusters in the hundred-kilodalton range (Arndt et al. 1999; Fein et al. 2019; Williams et al. 2024; Pedalino et al. 2026). These experiments provide increasingly sensitive tests of any additional stochastic or nonlinear process that would suppress spatial coherence beyond standard environmental decoherence (Bassi et al. 2013; Nimmrichter and Hornberger 2013).

This paper studies one such possibility: a phenomenological localization channel associated with a local geometric aperture scale. The terminology *Djamilar* is retained as a label for the postulated

microscopic filtration unit from which the aperture concept originated, but no microscopic derivation is assumed here. The present contribution is deliberately narrower than a theory of gravity or a microscopic theory of spacetime. It isolates a quantum open-system sector, states its assumptions, constructs a completely positive Markovian dynamics, maps it to measured observables, and derives experiment-specific constraints.

The central distinction is between two roles played by geometry. The physical radius or extension R of a mechanically bound system controls whether the localization channel is activated. The path separation Δx controls how strongly an already activated channel suppresses a particular spatial coherence. Confusing these roles produces incorrect mass-size scaling and can make a per-particle interference observable look like a collective center-of-mass measurement. We therefore formulate an explicit domain prescription: the elementary object to which the rate law is applied is a *maximal mechanically bound domain* whose internal relative coordinates remain localized on the experimental timescale. A molecule or stable cluster can form one domain; a dilute gas or a Bose-Einstein condensate is treated as a collection of atomic or molecular domains unless an independently demonstrated collective rigid mode is the measured degree of freedom.

The dynamics is written as a translation-covariant Lindblad generator, ensuring trace preservation and complete positivity (Lindblad 1976; Gorini, Kossakowski, and Sudarshan 1976). The model is phenomenological. Its normalization γ_0, mass exponent α, aperture scale r_d, and activation exponent p must be constrained rather than inferred from a desired transition. We take $r_d = 25\,\mathrm{nm}$, $\alpha = 1$, and $p = 4$ as a reference benchmark because it is the convention used throughout the numerical analysis. The value 25 nm is not described as an experimentally observed universal threshold.

Two complementary datasets are used. First, the localization kernel is inserted into the deposited raw-count analysis of the MUSCLE sodium-cluster Talbot-Lau experiment (Pedalino et al. 2026). The raw likelihood contains 95 scans and 3,895 phase points. Photophysical and interferometric calibration parameters are profiled or enveloped only where the primary data support a numerical treatment; no unpublished covariance matrix is invented. Second, the same generator is mapped to the differential acceleration spectrum of LISA Pathfinder (Armano, Audley, Auger, et al. 2018; Armano, Audley, Baird, et al. 2018; Armano et al. 2024), following the force-noise logic used to constrain collapse models (Helou et al. 2017). This combination tests both the numerical rate parameters and the structural assumption that a macroscopic test mass constitutes one localization domain.

The paper is organized as follows. Sections 2 and 3 define the aperture model, domain prescription, completely positive dynamics, diffusion, and scaling. Section 4 derives observable transfer functions. Sections 5 and 6 present the MUSCLE likelihood and the sodium-cluster rigidity assessment. Section 7 derives the LISA Pathfinder constraint. Section 8 combines the constraints and checks selected interference experiments. Section 9 gives a concrete first-order Talbot design target. Sections 10 and 11 state the limitations and falsifiable experimental program. Appendices collect the statistical, spectral, and numerical details required for reproducibility.

2. Phenomenological geometric-localization sector

2.1 Aperture scale and scope

We introduce r_d directly as the positive phenomenological spatial scale entering the localization kernel,

$$r_d > 0.$$

In this open-system model, r_d is constrained jointly with γ_0, α, and p. No microscopic origin, gravitational field equation, or environmental evolution law is assumed.

For the terrestrial numerical comparisons below, we use the benchmark

$$r_d = 25\,\mathrm{nm}.$$

This value is a reference convention, not an experimentally established universal threshold. The calculations therefore test only the localization generator defined in this paper and do not import the dynamics of a broader gravitational sector.

2.2 Rate law and activation

For a domain of mass M and physical radius or characteristic extension R, the geometric localization rate is postulated to be

$$\Gamma_D(M, R; r_d) = \gamma_0 \left(\frac{M}{m_0}\right)^{\alpha} \mathcal{F}_p\left(\frac{R}{r_d}\right),$$

where m_0 is the atomic mass unit, γ_0 has dimensions of inverse time, α is a mass-scaling exponent, and

$$\mathcal{F}_p(z) = \frac{z^p}{1+z^p}, \qquad p > 0.$$

The function is smooth, monotonic, and bounded. For $R \ll r_d$,

$$\mathcal{F}_p(R/r_d) \simeq (R/r_d)^p,$$

whereas for $R \gg r_d$ it saturates to unity. The exponent p is not derived by the present model. We retain it as a free structural parameter and use $p = 4$ as the principal numerical benchmark.

The mass and size factors are separated deliberately. The mass factor specifies amplification once a domain has been chosen. The activation factor tests whether the physical domain is small or large relative to the aperture. A cloud radius, interferometer arm separation, or apparatus dimension must not be inserted in place of the physical radius of the localization domain.

2.3 Domain prescription

A *maximal mechanically bound domain* is a connected bound component satisfying, over the experimental duration:

1. internal relative-coordinate fluctuations are small compared with the localization aperture relevant to the benchmark;
2. fragmentation or evaporation does not destroy the component;
3. irreversible rearrangements do not invalidate a single-domain description;
4. the measured observable actually probes the coherence of that domain.

The internal rigidity measure used here is the instantaneous root-mean-square relative-coordinate amplitude σ_{rel}. Accumulated drift, diffusion, rearrangement, and fragmentation are separate diagnostics. The condition $\sigma_{\mathrm{rel}} \ll r_d$ is sufficient for the benchmark but not by itself a microscopic proof of rigidity.

For nonspherical domains, R is taken to be a declared volume-equivalent or otherwise experiment-specific characteristic radius, and the spatial form factor should be retained when the shape materially affects the transfer function. No object is assigned a freely adjustable radius chosen to strengthen a bound.

2.4 Composite versus domain-wise localization

Consider a compact aggregate of N identical constituents, each of mass m_a and radius R_a, at fixed density. Then $M = Nm_a$ and $R_{\mathrm{comp}} \simeq N^{1/3} R_a$. Applying the rate law to one rigid composite gives

$$\Gamma_{\mathrm{comp}} = \gamma_0 \left(\frac{N m_a}{m_0} \right)^{\alpha} \mathcal{F}_p\!\left(\frac{N^{1/3} R_a}{r_d} \right),$$

whereas summing N independently localizing microscopic domains gives

$$\Gamma_{\mathrm{domains}} = N \gamma_0 \left(\frac{m_a}{m_0} \right)^{\alpha} \mathcal{F}_p\!\left(\frac{R_a}{r_d} \right).$$

Their ratio is

$$\frac{\Gamma_{\mathrm{comp}}}{\Gamma_{\mathrm{domains}}} = N^{\alpha-1} \frac{\mathcal{F}_p(N^{1/3} R_a / r_d)}{\mathcal{F}_p(R_a / r_d)}.$$

If both levels lie below the aperture, this becomes

$$\frac{\Gamma_{\mathrm{comp}}}{\Gamma_{\mathrm{domains}}} \simeq N^{\alpha-1+p/3}.$$

For $p = 4$ and $\alpha = 1$, the enhancement is $N^{4/3}$. If both levels are saturated, the ratio instead tends to $N^{\alpha-1}$ and is unity for $\alpha = 1$. The composite rule is therefore not a harmless convention: in the crossover regime it is the principal amplification mechanism and a directly falsifiable structural postulate.

3. Completely positive localization dynamics

3.1 Translation-covariant generator

Let $\hat{\mathbf{X}}$ be the center-of-mass position operator of one domain. A normalized isotropic Gaussian momentum-transfer density is

$$\mu_{r_d}(\mathbf{q}) = \frac{r_d^3}{\pi^{3/2} \hbar^3} \exp\!\left(-\frac{r_d^2 q^2}{\hbar^2} \right), \qquad \int d^3q \, \mu_{r_d}(\mathbf{q}) = 1.$$

The localization generator is

$$\mathcal{L}_D[\rho] = \Gamma_D \int d^3q\, \mu_{r_d}(\mathbf{q}) \left(e^{i\mathbf{q}\cdot\hat{\mathbf{X}}/\hbar} \rho e^{-i\mathbf{q}\cdot\hat{\mathbf{X}}/\hbar} - \rho \right).$$

This is a convex mixture of unitary momentum kicks and is therefore trace preserving and completely positive. With the Hamiltonian contribution included,

$$\frac{d\rho}{dt} = -\frac{i}{\hbar}[H, \rho] + \mathcal{L}_D[\rho].$$

In the position representation,

$$\frac{\partial \rho(\mathbf{x}, \mathbf{x}', t)}{\partial t} = -\frac{i}{\hbar}[H, \rho](\mathbf{x}, \mathbf{x}') - \Gamma_D \left[1 - \exp\left(-\frac{|\mathbf{x} - \mathbf{x}'|^2}{4r_d^2} \right) \right] \rho(\mathbf{x}, \mathbf{x}', t).$$

The diagonal $\rho(\mathbf{x}, \mathbf{x})$ is unchanged by the localization term. Coherences much smaller than r_d are weakly affected, while coherences much larger than r_d decay at the full rate Γ_D.

3.2 Momentum diffusion and heating

For $|\mathbf{x} - \mathbf{x}'| \ll r_d$, expanding the exponential gives

$$\mathcal{L}_D[\rho](\mathbf{x}, \mathbf{x}') \simeq -\frac{\Gamma_D}{4r_d^2} |\mathbf{x} - \mathbf{x}'|^2 \rho(\mathbf{x}, \mathbf{x}').$$

Using the one-axis white-force convention

$$\langle F_i(t) F_j(t') \rangle = D_C\, \delta_{ij} \delta(t - t'),$$

this corresponds to

$$D_C = \frac{\hbar^2 \Gamma_D}{2r_d^2}.$$

The three-dimensional kinetic-energy growth for a free domain is

$$\frac{d\langle E \rangle}{dt} = \frac{3D_C}{2M} = \frac{3\hbar^2 \Gamma_D}{4Mr_d^2}.$$

Thus the localization ansatz implies not only visibility loss but also momentum diffusion and heating. These observables provide independent constraints, including the force-noise bound from LISA Pathfinder derived in Section 7.

3.3 Size-scaling signature

At fixed mass density, $M \propto R^3$. In the sub-aperture regime,

$$\Gamma_D \propto R^{3\alpha + p},$$

while in the saturated regime,

$$\Gamma_D \propto R^{3\alpha}.$$

For the benchmark $\alpha = 1$, $p = 4$, the predicted slope changes from R^7 to R^3. In a Talbot-Lau experiment the flight time can itself depend on mass and size; the measured attenuation slope must therefore be computed with the apparatus transfer function rather than read directly from the bare rate. A size scan remains valuable because independent microscopic domains do not reproduce the same activation-induced crossover.

4. Mapping the channel to interferometers

4.1 General path-separation functional

For a coherence between two semiclassical paths separated by $\Delta\mathbf{x}(t)$, the localization attenuation exponent is

$$D_D = \Gamma_D \int dt \left[1 - \exp\left(-\frac{|\Delta\mathbf{x}(t)|^2}{4r_d^2}\right)\right].$$

The corresponding visibility factor is

$$\frac{V}{V_0} = e^{-D_D},$$

where V_0 is the visibility predicted by conventional propagation, environmental decoherence, calibration, and detection. The measured visibility cannot be identified with V_0. A statistically valid constraint must either model the baseline or profile physically motivated nuisance parameters using the complete measured pattern.

For a constant separation d over a duration T,

$$D_D = \Gamma_D T \left[1 - e^{-d^2/(4r_d^2)}\right].$$

For a linearly increasing separation from zero to $d_{\max}$, or a symmetric triangular path with total duration T, the time-averaged spatial factor is

$$K_{\mathrm{tri}} = 1 - \frac{\sqrt{\pi} r_d}{d_{\max}} \operatorname{erf}\left(\frac{d_{\max}}{2r_d}\right),$$

so that $D_D = \Gamma_D T K_{\mathrm{tri}}$.

4.2 Talbot-Lau transfer function

For a Talbot-Lau interferometer with grating period d, Talbot time

$$T_T = \frac{d^2 M}{h},$$

and free-evolution segments T_1 and T_2, the localization reduction of Fourier harmonic ℓ is

$$R_\ell^D = \exp\left[-\Gamma_D \sum_{i=1}^{2} T_i f(y_i)\right],$$

with

$$y_i = \frac{\ell\, d\, T_i}{\sqrt{2}\, r_d\, T_T},$$

and

$$f(y) = 1 - \sqrt{\frac{\pi}{2}}\,\frac{\mathrm{erf}(y/\sqrt{2})}{y}.$$

Here the square root acts on the numerical factor 2 only; equivalently, $y_i = (\ell d T_i/T_T)/(\sqrt{2}r_d)$. The regular limit is $f(y) = y^2/6 + O(y^4)$ for $y \to 0$. In the MUSCLE analysis, R_1^D multiplies the first Talbot-Lau harmonic before the mass and velocity averages are taken. This order matters because M, v, photophysics, and the Talbot phase are correlated in the forward model.

4.3 Statistical identifiability

A localization channel is identifiable only relative to a conventional model. Parameters governing source flux, velocity distribution, mass selection, optical phase, polarizability, photo-ionization, transmission, detector response, and global contrast efficiency can mimic part of a visibility loss. The appropriate likelihood is therefore schematically

$$p(\text{raw counts} \mid \gamma_0, r_d, \alpha, p, \theta_{\mathrm{TL}}, \eta_{\mathrm{cal}}),$$

where θ_{TL} denotes physical propagation parameters and η_{cal} denotes calibration parameters with independent information. A nuisance parameter is introduced only when its interpretation and allowed range are physically defensible. Parameters lacking published covariance information are not assigned arbitrary independent Gaussian priors.

5. MUSCLE sodium-cluster likelihood

5.1 Dataset and reproduction of the deposited analysis

MUSCLE observed matter-wave interference of sodium clusters in the mass range 143–197 kDa with an effective center near 172 kDa (Pedalino et al. 2026). The deposited analysis contains 95 interference scans and 3,895 raw phase points, with 41 points per scan. Re-executing the deposited macroscopicity analysis reproduces

$$\tau_{5\%} = 2.84 \times 10^{15}\,\mathrm{s}, \qquad \mu = \log_{10}(\tau_{5\%}/\mathrm{s}) = 15.45.$$

The likelihood uses the raw binomial counts. The display rescaling factor 0.78 discussed in connection with a figure is absent from the deposited Bayesian raw-count calculation and is not introduced in the present analysis.

The geometric-localization factor R_1^D is inserted in the first harmonic after calculating the Talbot-Lau coefficients and before averaging over the measured mass spectrum and velocity distribution. Direct numerical evaluation agrees with the vectorized implementation at relative differences below 1.1×10^{-15} for the validation points.

5.2 Nuisance treatment

The benchmark is

$$r_d = 25\,\mathrm{nm}, \qquad \alpha = 1, \qquad p = 4,$$

with sodium density $971\,\mathrm{kg\,m^{-3}}$ to match the deposited code convention. The continuously profiled nuisance parameters are:

- a global contrast efficiency $\eta \in [0, 1]$;
- a global fringe phase $\varphi \in [-\pi, \pi]$;
- ultraviolet polarizability per atom, with the published calibration $4.5 \pm 0.5\,\mathrm{\AA}^3$ in polarizability-volume convention;
- a global ionization scale constrained by the raw transmission response.

The published or measured source alternatives define a discrete sensitivity envelope: the deposited velocity setting $(158, 9)\,\mathrm{m\,s^{-1}}$, the rounded setting $(160, 10)\,\mathrm{m\,s^{-1}}$, relative width endpoints, and three high-power mass spectra. Beam power and waist calibrations are not added again as independent priors because they enter the same inferred photophysical products and the covariance required to avoid double counting is not published.

5.3 Profile result

The nominal conditional profile has a positive best point near

$$\hat{\gamma}_0 \simeq 0.20\,\mathrm{s^{-1}},$$

but $\gamma_0 = 0$ lies at $\Delta\chi^2 \simeq 2.03$. The positive optimum is therefore not a statistically secure detection. It reflects the conservative permission for residual contrast mismatch to enter the localization channel.

The nominal upper values are

$$\gamma_0 < 0.36324\,\mathrm{s^{-1}} \quad (\Delta\chi^2 = 2.71),$$

and

$$\gamma_0 < 0.36684\,\mathrm{s^{-1}} \quad (\Delta\chi^2 = 3.84).$$

The largest supported sensitivity result is obtained for the rounded published velocity setting,

$$\gamma_0 < 0.40475\,\mathrm{s^{-1}} \quad (\Delta\chi^2 = 2.71).$$

We therefore report the manuscript-safe conditional sensitivity value

$$\boxed{\gamma_0 < 0.41\,\mathrm{s}^{-1}}$$

for $r_d = 25\,\mathrm{nm}$, $\alpha = 1$, and $p = 4$. The exact conservative crossing $0.40475\,\mathrm{s}^{-1}$ is used in every derived ratio, α crossover, and r_d profile; $0.41\,\mathrm{s}^{-1}$ is only its rounded presentation value.

The nuisance optimum reaches the hard contrast-efficiency boundary $\eta = 1$ before the reported crossings: near $\gamma_0 = 0.353\,\mathrm{s}^{-1}$ for the nominal profile and $0.390\,\mathrm{s}^{-1}$ for the conservative velocity-envelope profile. The subsequent steep rise of $\Delta\chi^2$ is therefore boundary-driven. The values at $\Delta\chi^2 = 2.71$ and 3.84 are retained as conventional profile-sensitivity criteria, not as confidence limits with calibrated frequentist coverage. The regular asymptotic interpretation described by Cowan et al. (Cowan et al. 2011) is not guaranteed when a profiled nuisance estimator lies on a hard boundary. No coverage probability is claimed; establishing one would require a dedicated Monte Carlo or bounded-likelihood calibration. The result remains conditional on the published calibration model and the declared nuisance prescription and is not a reconstruction of an unpublished full calibration covariance.

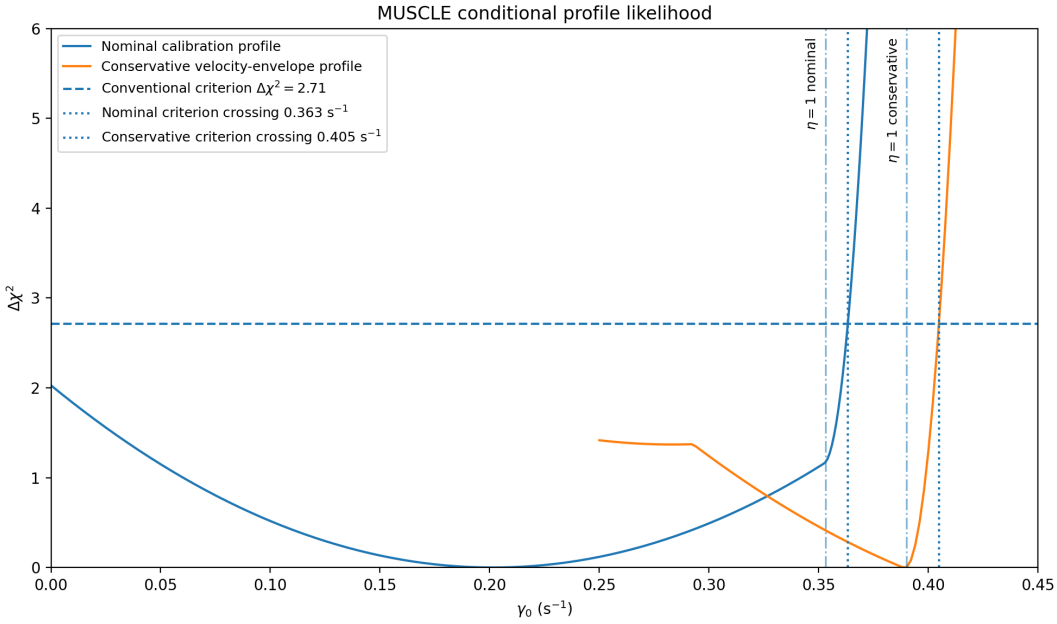

Figure 1: The profiled MUSCLE likelihood for the nominal calibration model and the conservative velocity-envelope branch. The dashed line is the conventional sensitivity criterion $\Delta\chi^2 = 2.71$, not a calibrated confidence threshold. Both profiles steepen after the contrast-efficiency nuisance reaches its hard boundary $\eta = 1$. The positive nominal optimum is not a secure detection because $\gamma_0 = 0$ remains below the conventional criterion.

The earlier fixed-calibration result $1.818 \times 10^{-2}\,\mathrm{s}^{-1}$ and the visibility proxy based on $-\ln(0.9)$ are reproducible historical intermediates but are not used as final bounds.

6. Mechanical-domain status of the sodium clusters

The MUSCLE constraint treats each selected sodium cluster as one maximal mechanically bound domain. This assumption must be checked rather than hidden inside the amplification factor.

The Supplementary Information, Sec. 2.4 (printed p. 6), assigns the clusters an internal temperature near 80 K and states that thermal evaporation of individual sodium atoms is negligible

(Pedalino et al. 2026). With grating separation $L = 0.98375\,\mathrm{m}$ and mean velocity near $160\,\mathrm{m\,s^{-1}}$, the time from the first to the third grating is

$$T_{\mathrm{exp}} = \frac{2L}{v} = 12.2969\,\mathrm{ms}.$$

As a vibration-scale comparator, Na^{+}_{139} has an equivalent Debye temperature $\Theta_D = 163.5 \pm 10\,\mathrm{K}$ (Sauceda, Garzon, and Michaelian 2013). The harmonic Debye estimate for one Cartesian component is evaluated and converted to a three-dimensional single-atom displacement. At 80 K it gives

$$u_{\mathrm{atom,RMS}} = 0.02513\,\mathrm{nm}.$$

For an intentionally conservative uncorrelated atomic pair,

$$\sigma_{\mathrm{rel}} = \sqrt{2}\,u_{\mathrm{atom,RMS}} = 0.03554\,\mathrm{nm},$$

so that

$$\frac{\sigma_{\mathrm{rel}}}{r_d} = 1.42 \times 10^{-3}$$

at $r_d = 25\,\mathrm{nm}$. A deliberately softened stress test with $\Theta_D = 100\,\mathrm{K}$ gives $\sigma_{\mathrm{rel}} = 0.05629\,\mathrm{nm}$ and $\sigma_{\mathrm{rel}}/r_d = 2.25 \times 10^{-3}$.

Studies of smaller sodium clusters place the onset of substantial surface mobility and homogeneous melting above the MUSCLE internal-temperature estimate (Aguado et al. 2001; Schmidt, Kusche, Hippler, et al. 2001; Schmidt, Kusche, Kronmuller, et al. 2001; Hock et al. 2011). These systems are not exact structural substitutes for 7,000–8,500-atom clusters, so they are used only as thermodynamic comparators.

We classify the rigid-domain approximation as *applicable under an explicit hypothesis*. The experimental temperature estimate, negligible evaporation, survival to mass detection, and small Debye displacement support the approximation over 12 ms. No direct in-flight diffraction or atomic-diffusion measurement exists for the selected clusters. The MUSCLE bound therefore remains conditional on this experimentally motivated rigidity assumption.

7. LISA Pathfinder force-noise constraint

7.1 Observable and spectral convention

LISA Pathfinder measured the residual differential acceleration $\Delta g(t)$ between two $1.928 \pm 0.001\,\mathrm{kg}$ Au-Pt test masses after calibration of actuation, stiffness, inertial motion, and geometric couplings (Armano, Audley, Auger, et al. 2018; Armano, Audley, Baird, et al. 2018). The principal low-noise band used here is 2–4 mHz, with central one-sided amplitude spectral density

$$S_{\Delta g}^{1/2} = 1.74 \times 10^{-15}\,\mathrm{m\,s^{-2}/\sqrt{Hz}}.$$

The later in-depth analysis confirms the one-sided spectral convention and details the windowing,

overlap, and glitch-purged datasets (Armano et al. 2024). The total residual spectrum is used as a conservative ceiling; no conventional noise component is subtracted. A stationary white localization force would not be removed as an isolated transient glitch.

7.2 Mapping to γ_0

For one mass and one Cartesian direction,

$$\langle F_i(t)F_j(t')\rangle = D_C\delta_{ij}\delta(t-t'), \qquad S_F^{(1)} = 2D_C.$$

If the two localization forces are independent and the masses are equal,

$$S_{\Delta g} = \frac{S_{F_1}^{(1)} + S_{F_2}^{(1)}}{M^2} = \frac{4D_C}{M^2}.$$

Therefore

$$D_C^{\max} = \frac{M^2 S_{\Delta g}}{4}.$$

Using $D_C = \hbar^2\Gamma_D/(2r_d^2)$ and the saturated $\alpha = 1$ rate $\Gamma_D = \gamma_0 M/m_0$ gives

$$\gamma_{0,\max} = \frac{M m_0 r_d^2 S_{\Delta g}}{2\hbar^2}.$$

At $r_d = 25\,\mathrm{nm}$,

$$\boxed{\gamma_{0,\max}^{\mathrm{LPF}} = 2.7236564 \times 10^{-4}\,\mathrm{s}^{-1}}$$

or $2.724 \times 10^{-4}\,\mathrm{s}^{-1}$ at manuscript precision. The quoted abstract ASD uncertainty is

$$\sigma_{\mathrm{ASD}} = 0.01\,\mathrm{fm\,s^{-2}\,Hz^{-1/2}}.$$

Combining it with the mass uncertainty gives approximately 1.15%. This is a measurement uncertainty only; it does not include the structural uncertainty of treating each macroscopic test mass as one domain or the assumption that the channel is white and Markovian in the selected band.

The bound constrains the pair (γ_0, macroscopic rigid-domain prescription). Decomposing a test mass into microscopic domains would drastically weaken it. The single-domain assumption is therefore experimentally consequential, not a bookkeeping choice.

8. Joint constraints and consistency checks

8.1 Dependence on the mass exponent

The MUSCLE values below use the exact conventional-criterion crossing $0.40475\,\mathrm{s}^{-1}$; the rounded $0.41\,\mathrm{s}^{-1}$ appears only in summary prose.

At $r_d = 25\,\mathrm{nm}$ and $p = 4$, the conservative MUSCLE and LPF upper normalizations at $\alpha = 1$ are

$$\gamma_{0,\mathrm{MUSCLE}} = 0.40475\,\mathrm{s}^{-1}, \qquad \gamma_{0,\mathrm{LPF}} = 2.7236564 \times 10^{-4}\,\mathrm{s}^{-1}.$$

Their ratio is

$$\frac{\gamma_{0,\mathrm{MUSCLE}}}{\gamma_{0,\mathrm{LPF}}} = 1486.054.$$

The profiles cross at

$$\boxed{\alpha_* = 0.854633}.$$

A calculation using the two effective masses gives 0.854689, confirming the full-profile interpolation. For $\alpha < \alpha_*$, the smaller MUSCLE mass loses less normalization leverage and its interferometric constraint becomes stronger. For $\alpha > \alpha_*$, the macroscopic LPF test masses dominate.

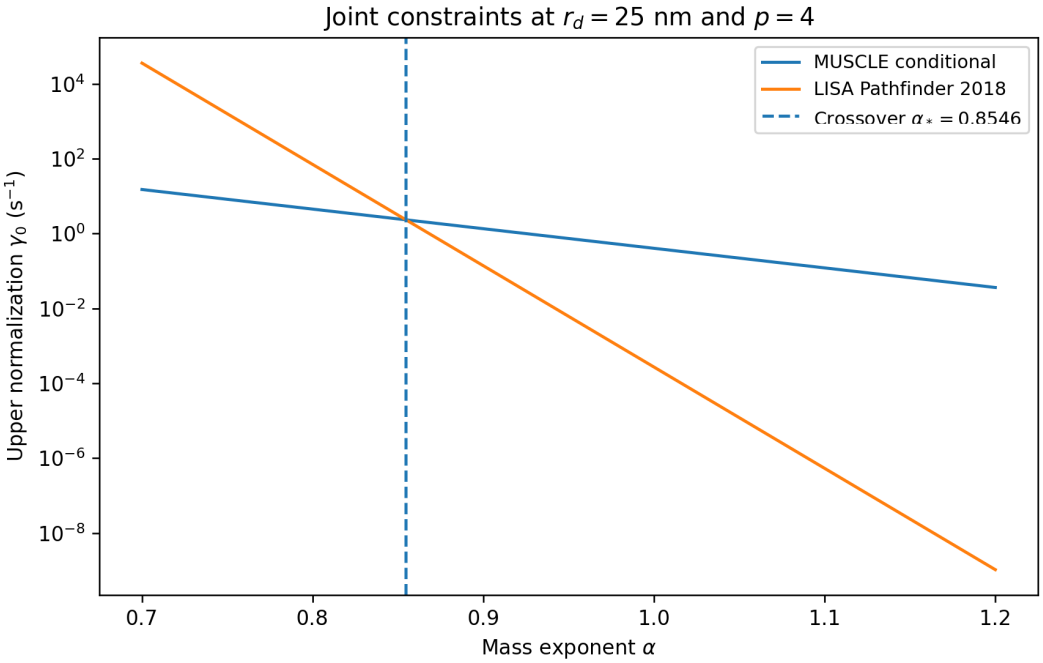

Figure 2: MUSCLE and LISA Pathfinder constraints as functions of the mass exponent at $r_d = 25\,\mathrm{nm}$ and $p = 4$. The crossing is conditional on applying the same rigid-domain rule in both experiments.

8.2 Dependence on aperture scale

The LPF result scales as $\gamma_{0,\max} \propto r_d^2$ in the saturated rigid-body limit. The MUSCLE curve is obtained by re-evaluating the full 3,895-point likelihood at each r_d and anchoring the conservative branch to $0.40475\,\mathrm{s}^{-1}$ at 25 nm. Selected values for $\alpha = 1$ and $p = 4$ are shown below.

r_d (nm)	MUSCLE γ_0 at $\Delta\chi^2 = 2.71$ (s^{-1})	LPF upper γ_0 (s^{-1})	MUSCLE/LPF
5	6.0132×10^{-4}	1.0895×10^{-5}	55.19
10	7.3761×10^{-3}	4.3579×10^{-5}	169.26

r_d (nm)	MUSCLE γ_0 at $\Delta\chi^2 = 2.71$ (s^{-1})	LPF upper γ_0 (s^{-1})	MUSCLE/LPF
25	4.0475×10^{-1}	2.7237×10^{-4}	1486.05
50	1.3777×10^{1}	1.0895×10^{-3}	1.2645×10^{4}
100	7.0501×10^{2}	4.3579×10^{-3}	1.6178×10^{5}

At the equivalent 172-kDa sodium radius $R = 4.1256\,\mathrm{nm}$, the ratio is 50.849. The old proxy values are not used.

The asymptotic combinations useful for comparing experiments are

$$\beta_{\mathrm{int}} = \frac{\gamma_0}{r_d^p}, \qquad \beta_{\mathrm{LPF}} = \frac{\gamma_0}{r_d^2}.$$

At 25 nm and $p = 4$, the exact conservative values are

Combination	MUSCLE	LPF 2018
γ_0/r_d^4 (s^{-1} nm^{-4})	1.03616×10^{-6}	6.97256×10^{-10}
γ_0/r_d^2 (s^{-1} nm^{-2})	6.47600×10^{-4}	4.35785×10^{-7}

8.3 Selected experiment-specific consistency checks

The purpose of this table is not to assert universal non-refutation. Each row uses the observable and domain prescription of one identified experiment. Atomic ensembles are treated per particle; the cloud radius and atom number do not define a rigid composite domain.

System	Domain and primary input	Attenuation exponent under LPF 2018	Reading
C60 diffraction (Arndt et al. 1999; Liu et al. 1991)	One 720-Da molecule; $R = 0.35325$ nm; 5.682 ms	4.44×10^{-11}	Negligible
LUMI oligoporphyrins (Fein et al. 2019)	One molecule; representative mass 26,777 Da; 7.5 ms	Not assigned	Qualitative only; no unique primary structural radius
Rb-87 Cold Atom Lab (Williams et al. 2024)	One atomic domain; 1-ms sequence	1.41×10^{-13}	Negligible; no cloud-N amplification
Cs-133 fountain (Peters, Chung, and Chu 1999)	One atomic domain; 320-ms sequence	1.05×10^{-10}	Negligible; no cloud-size activation

For C60, the declared radius is half the measured mean atom-to-atom diameter 7.065(3) Å (Liu et al. 1991), not an unlabelled volume radius. For the Rb and Cs entries, covalent-radius conventions are used only to quantify the very small sub-aperture activation. The result is insensitive to modest atomic-radius conventions at the level relevant here. The LUMI row is intentionally not assigned a localization number because the molecular library does not provide a unique primary volume-equivalent radius.

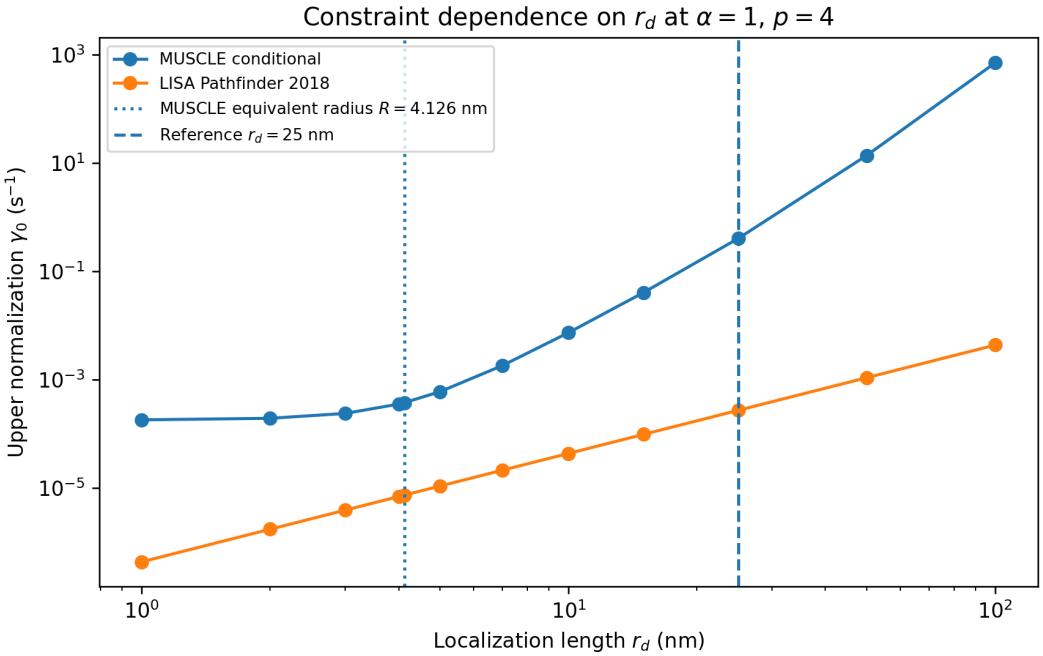

Figure 3: Dependence of the two upper normalizations on r_d at $\alpha = 1$ and $p = 4$. The MUSCLE curve is produced from complete likelihood profiles rather than a fixed-visibility proxy.

9. First-order Talbot design reach

A future matter-wave test should be designed with an explicit target attenuation rather than an arbitrary tolerance relative to the measured visibility. We use

$$D_D = 1$$

as a transparent design criterion: the geometric channel would reduce the corresponding harmonic by e^{-1} before conventional losses.

For a symmetric first-order Talbot-Lau geometry with grating period $d = 133\,\mathrm{nm}$, separation $L = 0.98375\,\mathrm{m}$, sodium density $971\,\mathrm{kg\,m^{-3}}$, $r_d = 25\,\mathrm{nm}$, $\alpha = 1$, $p = 4$, and the LPF upper normalization, the equality $D_D = 1$ occurs at

$$\boxed{D_{\mathrm{eq}} = 18.30095\,\mathrm{nm}}.$$

The corresponding parameters are

$$M_{\mathrm{eq}} = 1.87668\,\mathrm{MDa},$$

$$v_{\mathrm{eq}} = 11.8249\,\mathrm{m\,s^{-1}},$$

$$T_{\mathrm{tot}} = \frac{2L}{v_{\mathrm{eq}}} = 0.166386\,\mathrm{s},$$

and the gravitational drop over this duration is

$$\frac{1}{2} g T_{\mathrm{tot}}^2 = 13.5745\,\mathrm{cm}.$$

The large drop is an engineering constraint, not a theoretical inconsistency. It motivates vertical compensation, a modified geometry, microgravity operation, or higher Talbot order. The gain D_D evaluated at the LPF normalization is 0.01491, 0.06944, and 2.4116 for diameters 12, 14, and 20 nm, respectively.

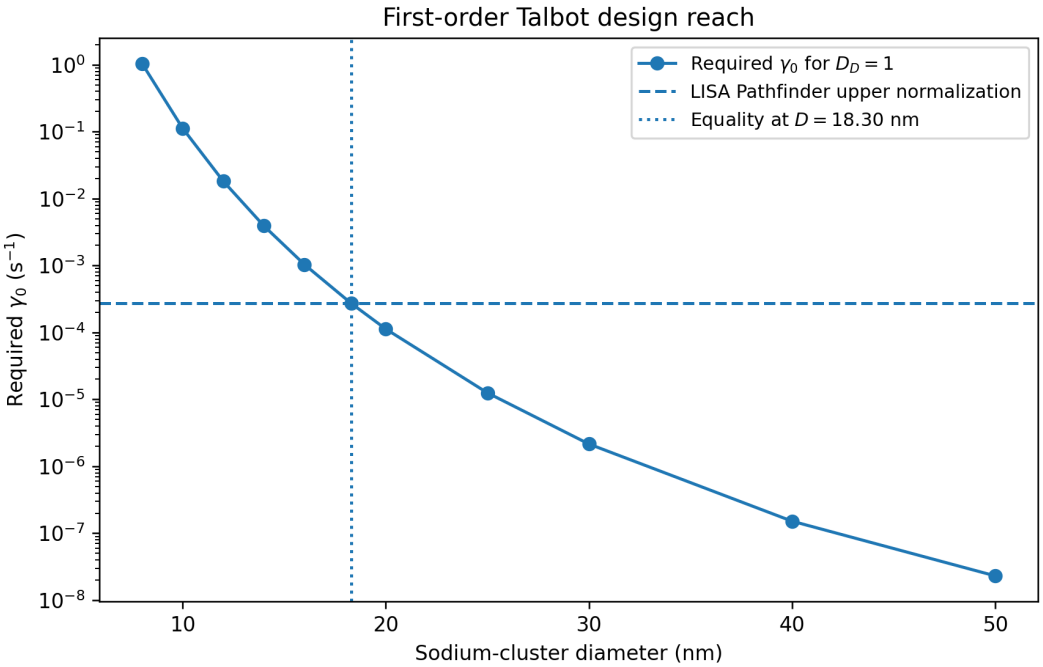

Figure 4: Required normalization for a first-order sodium-cluster Talbot design to reach $D_D = 1$. The intersection with the LISA Pathfinder upper normalization occurs at $D = 18.30\,\mathrm{nm}$.

The target is conditional on the first-order geometry and the rigid-cluster prescription. It is not a forecast of guaranteed visibility, because source flux, conventional decoherence, grating response, mass selection, and detector efficiency must also be propagated.

10. Discussion and limitations

10.1 What is constrained

The analysis constrains the explicit phenomenological generator defined in Sections 2 and 3. The numerical statements do not establish any particular microscopic spacetime-filtration unit or discrete mesh. A null result constrains γ_0 only together with r_d, α, p, the domain prescription, and the assumed spectral character of the stochastic channel.

The strongest benchmark result comes from LISA Pathfinder, not MUSCLE. This hierarchy is a consequence of the linear mass scaling and the macroscopic single-domain assumption. If the localization field couples only to microscopic domains within a test mass, the LPF bound can become effectively nonconstraining. Conversely, MUSCLE is directly sensitive to the composite-domain crossover and remains crucial for testing the structural amplification itself.

10.2 Conditional nature of the MUSCLE result

The MUSCLE upper value is a conditional conventional-criterion sensitivity result, not a coverage-calibrated confidence limit. The raw likelihood, mass and velocity averages, and declared calibration information are reproduced. A complete experimental covariance among laser power, waist, polarizability, ionization, transmission, source variations, and detector response is not publicly available. The analysis avoids claiming that such a covariance has been reconstructed. New calibration information could strengthen or weaken the bound.

The positive nominal profile optimum should not be interpreted as evidence. It is statistically compatible with zero and is sensitive to how residual contrast mismatch is distributed among calibration and localization parameters.

10.3 Domain uncertainty

The maximal mechanically bound domain is an additional postulate. The sodium-cluster rigidity check supports its use under an explicit temperature assumption, while atomic interferometers require a per-particle prescription. LISA Pathfinder tests the extrapolation of the same rule to a centimeter-scale solid. A future experiment that varies physical cluster size while holding conventional parameters under control can distinguish the rigid-composite slope from a sum over microscopic domains.

10.4 Markovian and Gaussian assumptions

The generator is Markovian, isotropic, and Gaussian in momentum transfer. These choices are sufficient to ensure complete positivity and yield a simple aperture kernel. They are not uniquely selected by the underlying geometric idea. Colored noise, anisotropic kernels, non-Gaussian jumps, dissipative completion, or non-Markovian memory would modify both the spectral and interferometric mappings. The LPF bound is applied only in the 2–4 mHz band and must not be extrapolated to arbitrary frequency without a spectral model.

10.5 Heating and radiation

The model predicts momentum diffusion and heating. These are not optional side effects: they follow from the same generator. The present LPF analysis uses force noise, while additional mechanical-heating data could supply complementary constraints.

No strong electromagnetic-radiation cancellation claim is used. A rigid translation of a neutral body suppresses the leading electric-dipole contribution, but multipolar, internal, electronic, and retardation effects require a separate electrodynamic calculation. Such a calculation is a future test rather than a missing numerical input to the bounds reported here.

10.6 Relation to collapse models

The generator has mathematical similarities to spatial-localization models, but no universal parameter map to CSL, GRW, or Diosi-Penrose dynamics is asserted (Bassi et al. 2013). The activation law, domain prescription, and geometric aperture are model-specific. Comparisons should be made at the observable level in a common geometry and spectral convention, as in the LISA Pathfinder treatment of collapse-induced force noise (Helou et al. 2017).

11. Falsifiable experimental program

The model can be tested by separating normalization, activation, composition, and environment.

Size scan. At fixed density and controlled velocity, the bare rate changes from $R^{3\alpha+p}$ to $R^{3\alpha}$. The apparatus transfer function modifies the measured slope but does not erase the characteristic crossover if sufficient size range and calibration precision are available.

Composition scan. Compare a rigid aggregate with an equivalent collection of independently propagating constituents. In the sub-aperture benchmark, the composite-to-domain enhancement $N^{\alpha-1+p/3}$ is the defining structural prediction.

Path-separation scan. Vary the maximum coherence separation at fixed mass and size. The kernel $1-\exp[-\Delta x^2/(4r_d^2)]$ predicts a specific saturation curve distinct from a simple constant visibility loss.

Temperature scan. At fixed size, thermal-emission decoherence changes strongly with internal temperature, while the present geometric rate has no explicit temperature dependence. Temperature remains indirectly relevant through density, fragmentation, source flux, and rigidity; those changes must be monitored rather than absorbed into the localization channel.

Cross-platform test. A common parameter set must describe both interferometric attenuation and force-noise/heating observables. A claimed signal in one platform that violates the LPF mapping or the diffusion relation would falsify the minimal generator.

Failure criteria. The benchmark sector is ruled out if null results exclude the full parameter region consistent with the common domain prescription, or if the observed size, separation, frequency, or composition dependence is incompatible with the predicted kernels. Conversely, an unexplained visibility loss at one point is insufficient evidence; a reproducible multidimensional signature is required.

12. Conclusion

We have formulated a geometric-localization ansatz as a completely positive open-system model and confronted it with raw matter-wave data and precision force-noise measurements. The rate law separates mass amplification from physical-size activation and requires an explicit mechanically bound-domain prescription. The resulting generator predicts spatial decoherence, momentum diffusion, heating, and a characteristic size crossover.

A reproduction and extension of the deposited MUSCLE likelihood yields no secure localization signal and gives the conditional conservative benchmark sensitivity value

$$\gamma_0 < 0.41\,\mathrm{s}^{-1}$$

at $r_d = 25\,\mathrm{nm}$, $\alpha = 1$, and $p = 4$. Under a white, independent-force, macroscopic rigid-domain interpretation, LISA Pathfinder gives

$$\gamma_0 < 2.724 \times 10^{-4}\,\mathrm{s}^{-1}.$$

The two constraints cross at $\alpha_* = 0.8546$. Existing C60, Rb, and Cs interference experiments remain consistent with the stronger bound under experiment-specific domain rules. A first-order

sodium-cluster design reaches $D_D = 1$ near 18.30 nm diameter, but requires slow particles and substantial gravitational compensation.

The results establish an auditable constraint program, not evidence for geometric microstructure. The decisive next step is a controlled size-, separation-, and temperature-resolved matter-wave experiment whose conventional forward model and calibration covariance are independently validated.

Data, code, and reproducibility

The complete reproducibility archive is provided as Supplementary Data accompanying this submission under the filename `Djamilar_global_recalculation_package_v2.zip`, with SHA-256 checksum

`d92e821365e2250f4f6bc7bfff5b0f2d156667d16842c7258fb588bcacdd93d1`.

It contains the closed MUSCLE, LISA Pathfinder, sodium-rigidity, and comparative-experiment packages; the full r_d profiles; the α curves; the Talbot design table; experiment-specific consistency calculations; figures; source code; and file-level checksums. The original MUSCLE article and supplementary information are available through DOI 10.1038/s41586-025-09917-9 (Pedalino et al. 2026).

Appendix A. Numerical status table

Quantity	Final value or rule	Scientific status
r_d	25 nm benchmark	Reference scale, not universal measured threshold
p	Free; $p = 4$ benchmark	Structural model parameter
α	Free; $\alpha = 1$ benchmark	Mass-scaling parameter
MUSCLE γ_0	$< 0.41\,\mathrm{s}^{-1}$	Conditional conventional-criterion value; coverage not calibrated
LPF γ_0	$< 2.724 \times 10^{-4}\,\mathrm{s}^{-1}$	Conditional white-force bound
MUSCLE rigidity	Applicable under explicit hypothesis	No direct in-flight structural measurement
Domain rule	Maximal mechanically bound component	Falsifiable additional postulate
LUMI attenuation exponent	Not assigned	No unique primary structural radius
Radiation cancellation	Not used quantitatively	Detailed calculation deferred
Old $-\ln(0.9)$ proxy	Rejected as bound	Historical illustration only

Appendix B. Selected r_d profile values

r_d (nm)	MUSCLE $\gamma_{0,\Delta\chi^2=2.71}$ (s^{-1})	LPF $\gamma_{0,\max}$ (s^{-1})	Ratio
1	1.81357×10^{-4}	4.35785×10^{-7}	416.16

r_d (nm)	MUSCLE $\gamma_{0,\Delta\chi^2=2.71}$ (s^{-1})	LPF $\gamma_{0,\max}$ (s^{-1})	Ratio
2	1.93863×10^{-4}	1.74314×10^{-6}	111.21
3	2.38419×10^{-4}	3.92207×10^{-6}	60.79
4	3.54784×10^{-4}	6.97256×10^{-6}	50.88
4.1256	3.77163×10^{-4}	7.41731×10^{-6}	50.849
5	6.01315×10^{-4}	1.08946×10^{-5}	55.19
7	1.82239×10^{-3}	2.13535×10^{-5}	85.344
10	7.37611×10^{-3}	4.35785×10^{-5}	169.26
15	4.06819×10^{-2}	9.80516×10^{-5}	414.90
25	4.04750×10^{-1}	2.72366×10^{-4}	1486.05
50	1.37773×10^{1}	1.08946×10^{-3}	1.2646×10^{4}
100	7.05009×10^{2}	4.35785×10^{-3}	1.6178×10^{5}

Appendix C. First-order Talbot design table

Diameter (nm)	Mass (MDa)	Velocity (m s^{-1})	Total time (s)	D_D at LPF bound	Vertical drop
12	0.529069	41.9446	0.046907	0.014906	1.0789 cm
14	0.840142	26.4141	0.074487	0.069440	2.7205 cm
16	1.254090	17.6954	0.111187	0.262820	6.0618 cm
18.30095	1.87668	11.8249	0.166386	1.0000	13.5745 cm
20	2.449395	9.06003	0.217163	2.41163	23.1239 cm
25	4.783974	4.63874	0.424146	21.6801	88.2106 cm

The table is a design calculation under the stated first-order geometry. Values are not experimental exclusions.

References

Aguado, Andres, Jose M. Lopez, Julio A. Alonso, and Malcolm J. Stott. 2001. "Melting in Large Sodium Clusters: An Orbital-Free Molecular Dynamics Study." *Journal of Physical Chemistry B* 105: 2386–92. https://doi.org/10.1021/jp0018504.

Armano, M. et al. 2024. "In-Depth Analysis of LISA Pathfinder Performance Results." *Physical Review D* 110: 042004. https://doi.org/10.1103/PhysRevD.110.042004.

Armano, M., H. Audley, G. Auger, et al. 2018. "Beyond the Required LISA Free-Fall Performance: New LISA Pathfinder Results down to 20 Microhertz." *Physical Review Letters* 120: 061101. https://doi.org/10.1103/PhysRevLett.120.061101.

Armano, M., H. Audley, J. Baird, et al. 2018. "Calibrating the System Dynamics of LISA Pathfinder." *Physical Review D* 97: 122002. https://doi.org/10.1103/PhysRevD.97.122002.

Arndt, Markus, Olaf Nairz, Julian Vos-Andreae, Claudia Keller, Gerbrand van der Zouw, and Anton Zeilinger. 1999. "Wave-Particle Duality of C60 Molecules." *Nature* 401: 680–82. https://doi.org/10.1038/44348.

Bassi, Angelo, Kinjalk Lochan, Seema Satin, Tejinder P. Singh, and Hendrik Ulbricht. 2013. "Models of Wave-Function Collapse, Underlying Theories, and Experimental Tests." *Reviews of Modern Physics* 85: 471–527. https://doi.org/10.1103/RevModPhys.85.471.

Cowan, Glen, Kyle Cranmer, Eilam Gross, and Ofer Vitells. 2011. "Asymptotic Formulae for Likelihood-Based Tests of New Physics." *European Physical Journal C* 71: 1554. https://doi.org/10.1140/epjc/s10052-011-1554-0.

Fein, Yaakov Y., Philipp Geyer, Patrick Zwick, et al. 2019. "Quantum Superposition of Molecules Beyond 25 kDa." *Nature Physics* 15: 1242–45. https://doi.org/10.1038/s41567-019-0663-9.

Gorini, Vittorio, Andrzej Kossakowski, and E. C. G. Sudarshan. 1976. "Completely Positive Dynamical Semigroups of n-Level Systems." *Journal of Mathematical Physics* 17: 821–25. https://doi.org/10.1063/1.522979.

Helou, Bassam, Bram J. J. Slagmolen, David E. McClelland, and Yanbei Chen. 2017. "LISA Pathfinder Appreciably Constrains Collapse Models." *Physical Review D* 95: 084054. https://doi.org/10.1103/PhysRevD.95.084054.

Hock, Christian, Christian Bartels, Stefan Straßburg, Martin Schmidt, Hellmut Haberland, and Bernd von Issendorff. 2011. "Low-Temperature Caloric Behavior of a Free Sodium Nanoparticle." *Physical Review B* 84: 113401. https://doi.org/10.1103/PhysRevB.84.113401.

Lindblad, Goran. 1976. "On the Generators of Quantum Dynamical Semigroups." *Communications in Mathematical Physics* 48: 119–30. https://doi.org/10.1007/BF01608499.

Liu, S., Y.-J. Lu, M. M. Kappes, and J. A. Ibers. 1991. "The Structure of the C60 Molecule: X-Ray Crystal Structure Determination of a Twin at 110 k." *Science* 254: 408–10. https://doi.org/10.1126/science.254.5030.408.

Nimmrichter, Stefan, and Klaus Hornberger. 2013. "Macroscopicity of Mechanical Quantum Superposition States." *Physical Review Letters* 110: 160403. https://doi.org/10.1103/PhysRevLett.110.160403.

Pedalino, S., B. E. Ramirez-Galindo, R. Ferstl, et al. 2026. "Probing Quantum Mechanics with Nanoparticle Matter-Wave Interferometry." *Nature* 649: 866–70. https://doi.org/10.1038/s41586-025-09917-9.

Peters, Achim, Keng Yeow Chung, and Steven Chu. 1999. "Measurement of Gravitational Acceleration by Dropping Atoms." *Nature* 400: 849–52. https://doi.org/10.1038/23655.

Sauceda, Huziel E., Ignacio L. Garzon, and Karo Michaelian. 2013. "Vibrational Spectrum, Caloric Curve, Low-Temperature Heat Capacity, and Debye Temperature of Sodium Clusters: The Na139+ Case." *Journal of Physical Chemistry C* 117: 11393–98. https://doi.org/10.1021/jp401903f.

Schmidt, Martin, Robert Kusche, Thomas Hippler, Joern Donges, Wolfgang Kronmuller, Bernd von Issendorff, and Hellmut Haberland. 2001. "Negative Heat Capacity for a Cluster of 147 Sodium Atoms." *Physical Review Letters* 86: 1191–94. https://doi.org/10.1103/PhysRevLett.86.1191.

Schmidt, Martin, Robert Kusche, Wolfgang Kronmuller, Bernd von Issendorff, and Hellmut Haberland. 2001. "Caloric Curve Across the Liquid-to-Gas Change for Sodium Clusters." *Physical Review Letters* 87: 203402. https://doi.org/10.1103/PhysRevLett.87.203402.

Williams, Jason et al. 2024. "Pathfinder Experiments with Atom Interferometry in the Cold Atom Lab Onboard the International Space Station." *Nature Communications* 15: 6414. https://doi.org/10.1038/s41467-024-50585-6.